

# Actron3D: Learning Actionable Neural Functions from Videos for Transferable Robotic Manipulation

Anran Zhang<sup>\*,1,2</sup> Hanzhi Chen<sup>\*,1,2</sup> Yannick Burkhhardt<sup>1,2</sup> Yao Zhong<sup>2</sup>

Johannes Betz<sup>2</sup> Helen Oleynikova<sup>1</sup> Stefan Leutenegger<sup>1</sup>

\* Equal Contribution <sup>1</sup> ETH Zurich <sup>2</sup> Technical University of Munich

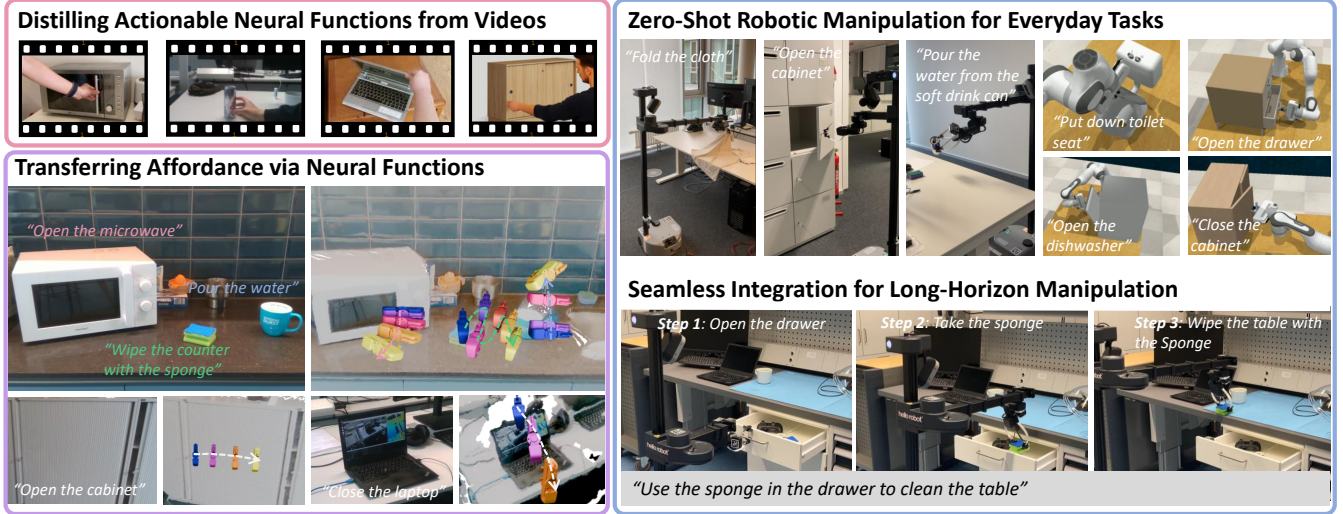


Fig. 1: *Actron3D* is a framework distilling actionable cues from diverse video sources—casual recordings, HOI datasets, or generated contents—into continuous neural representations, enabling transfer manipulation skills to novel scenarios. Project website: <https://dipan-zhang.github.io/Actron3D-project/>

**Abstract**—We present ACTRON3D, a framework that enables robots to acquire transferable 6-DoF manipulation skills from just a few monocular, uncalibrated, RGB-only human videos. At its core lies the *Neural Affordance Function*, a compact object-centric representation that distills actionable cues from diverse uncalibrated videos—geometry, visual appearance, and affordance—into a lightweight neural network, forming a memory bank of manipulation skills. During deployment, we adopt a pipeline that retrieves relevant affordance functions and transfers precise 6-DoF manipulation policies via coarse-to-fine optimization, enabled by continuous queries to the multimodal features encoded in the neural functions. Experiments in both simulation and the real world demonstrate that ACTRON3D significantly outperforms prior methods, achieving a 14.9 percentage point improvement in average success rate across 13 tasks while requiring only 2–3 demonstration videos per task.

## I. INTRODUCTION

Building a generalist robot remains challenging. Such an agent must acquire interaction skills and transfer them to unseen objects and environments across embodiments. In stark contrast to the contemporary data-hungry robotics systems, humans provide a powerful example of efficient learning: Infants, for example, can learn tasks like opening a cabinet by observing a few demonstrations and then readily transfer this knowledge to similar instances [1].

Recent approaches [2–4] follow this direction by leveraging out-of-domain data such as human videos to predict or transfer affordance trajectories in pixel space. While this improves sample efficiency, the absence of explicit 3D

reasoning leads to ambiguity when lifting pixel predictions into spatially grounded actions, even with local geometric priors. To overcome this, another line of work extracts 3D actionable cues from human videos, such as point flows [5, 6] or 3D waypoints [7, 8]. Yet these methods still face key challenges: they often depend on manually specified contact points or goal images, or cannot reliably infer robot gripper orientations. Most critically, under domain shifts, e.g., unseen objects or large viewpoint mismatches between human- and robot-centric observations, their performance deteriorates, leading to substantial performance drops as shown in [7].

Videos offer a rich medium for robot learning: they are ubiquitous, informative, and actionable. However, the discussed limitations of prior approaches motivate two central questions in this work: (1) How can we distill compact, actionable information from videos into representations that transfer reliably across embodiments, object instances, and viewpoints? (2) How can such representations be effectively adapted and executed in novel scenarios? To this end, we propose ACTRON3D, a *distill-then-transfer* framework that achieves zero-shot robotic manipulation with high sample efficiency. In the *distillation* phase, ACTRON3D converts information-rich videos into compact neural representations, *Neural Affordance Functions*, that capture actionable cues at multiple levels—geometry, visual appearance, and affordance. The input videos are uncalibrated and may come from diverse sources, including casually recorded clips, human-

object interaction datasets [9], or generated content [10]. In the *transfer* phase, the robot retrieves the most relevant neural representation from a memory bank, aligns it with the target object through our formulated coarse-to-fine differentiable affordance optimization, and produces a precise 6-DoF manipulation trajectory, enabling zero-shot policy deployment. Representing manipulation skills as differentiable neural functions is inspired by the *render-and-compare* optimization paradigm in SLAM and computer graphics, where attributes such as camera poses are recovered by iteratively aligning observations with renderings [11–13]. In robotic manipulation, actions lie in a much higher-dimensional space and demand finer precision, whereas prior works typically transfer motor skills via *one-step feature matching* with visual or geometric descriptors [3, 4, 14]. In contrast, our representation enables consistent *iterative cross-modal alignment*, allowing robot actions to be derived through optimization within a continuous energy landscape.

We evaluate ACTRON3D through extensive simulation and real-world experiments. With only 2–3 demonstration videos per task, it outperforms several data-hungry baselines [4, 7, 15–17] by a 14.9 percentage point (pp) improvement in average success rate across 13 tasks.

In summary, our main contributions are: (1) A novel 3D neural representation that distills actionable cues through *Neural Affordance Function* from a given uncalibrated video. (2) An effective pipeline for robust zero-shot transfer of 6-DoF manipulation skills via differentiable alignment. (3) Comprehensive experiments and downstream applications in both simulation and real-robot settings that validate the effectiveness and versatility of ACTRON3D.

## II. RELATED WORK

**Robotic Affordance Grounding.** Affordance refers to the actionable properties of objects, indicating where and how an agent should interact with them. Early works [18–20] focused on learning 2D affordance from human-annotated datasets via end-to-end training. However, their dependence on manual annotation limits scalability and hinders generalization to unseen environments. To overcome this, recent approaches [3, 4] leverage out-of-domain human videos to transfer affordance knowledge. However, these methods operate solely in the 2D image plane and lack 3D spatial grounding. Moreover, they typically rely on large, manually curated memory banks, increasing system complexity. Another direction [17, 21, 22] explores 3D affordance learning in simulation. While more spatially expressive, these methods require extensive synthetic assets and suffer from sim-to-real transfer challenges. In contrast, our method infers spatially grounded affordance using a compact memory bank of casually captured or generated videos, enabling zero-shot transfer without extensive annotations or simulation.

**Visual Features for Robotic Manipulation.** Recent advances have employed visual descriptors from foundation models to enable language-guided, context-aware robotic manipulation. A prominent line of work uses these descriptors for keypoint-based object correspondence [3, 4, 23],

supporting generalization from in-the-wild human demonstrations. However, the lack of 3D spatial grounding makes these methods sensitive to viewpoint changes. To improve robustness, several approaches [24–28] lift 2D features into 3D fields via differentiable rendering across multi-view captures. These 3D-grounded features serve as spatially consistent intermediates for policy learning or as matching costs for action planning. Yet, the reliance on controlled multi-view setups limits their scalability to unconstrained environments. In contrast, leveraging recent advances in novel view synthesis [29, 30], our approach reconstructs coherent 3D fields from monocular videos. These fields jointly encode multimodal, action-related features, enabling robust affordance transfer to novel objects and viewpoints without requiring complex capture setups.

**Robot Learning from Videos.** Previous works have explored various video sources to guide robot learning of manipulation skills. One line of research leverages human videos to learn visual representations [5, 31, 32] or reward functions [16, 33], thereby facilitating visuomotor policy learning. Another line utilizes MoCap systems to re-target human motions into the robot’s action space [8, 34–36]. However, these approaches are often limited to controlled lab settings due to infrastructure requirements. More recent methods attempt to infer affordance directly from large-scale human videos on the web [6, 7, 15, 37], but they face several limitations: they often require manual specification of contact points or goal images, or reduce interactions to sequences of 3D waypoints. Such simplifications make it difficult to perform more dexterous tasks, such as water pouring. Recent advances in generative video models have enabled robots to visually imagine actions, thereby expanding the types of video data usable for policy learning. For example, works like [38–40] infer robot policies conditioned on synthesized videos of human interactions. However, video generation at test time can be highly computationally expensive. In contrast, we propose a scalable framework to distill manipulation skills from diverse videos into several object-centric representations, enabling the robot to efficiently retrieve 6-DoF interaction trajectories from these representations without extensive demonstration or generation.

## III. METHOD

### A. Problem Formulation

Our framework to infer a manipulation policy is formulated as:  $\mathcal{T} = \pi_{\mathcal{V}}(\{\mathbf{I}, \mathbf{D}\}, l)$ , where  $\{\mathbf{I}, \mathbf{D}\}$  is an RGB-D observation and  $l$  is a natural language instruction. The output policy  $\mathcal{T} = \{\mathbf{T}_i\}_{i=1}^H$  is a sequence of 6-DoF gripper poses over a planning horizon  $H$ . Our approach uses a video memory bank  $\mathcal{V} = \{(\hat{V}_i, \hat{l}_i)\}_{i=1}^{N_{\mathcal{V}}}$ , where each video  $\hat{V}_i$  is paired with a narration  $\hat{l}_i$  describing the interaction. We first introduce a module  $\mathcal{G}_{\text{act}}$  that *distills* each video into an object-centric neural representation  $F_i = \mathcal{G}_{\text{act}}(\hat{V}_i, \hat{l}_i)$ , encoding actionable information (Sect. III-C). Collectively, these functions form a function memory bank  $\mathcal{M} = \{F_i\}_{i=1}^{N_{\mathcal{V}}}$ . To perform policy inference on a new observation  $(\{\mathbf{I}, \mathbf{D}\}, l)$ , we further introduce a second module  $\mathcal{G}_{\text{map}}$ , which *transfers*

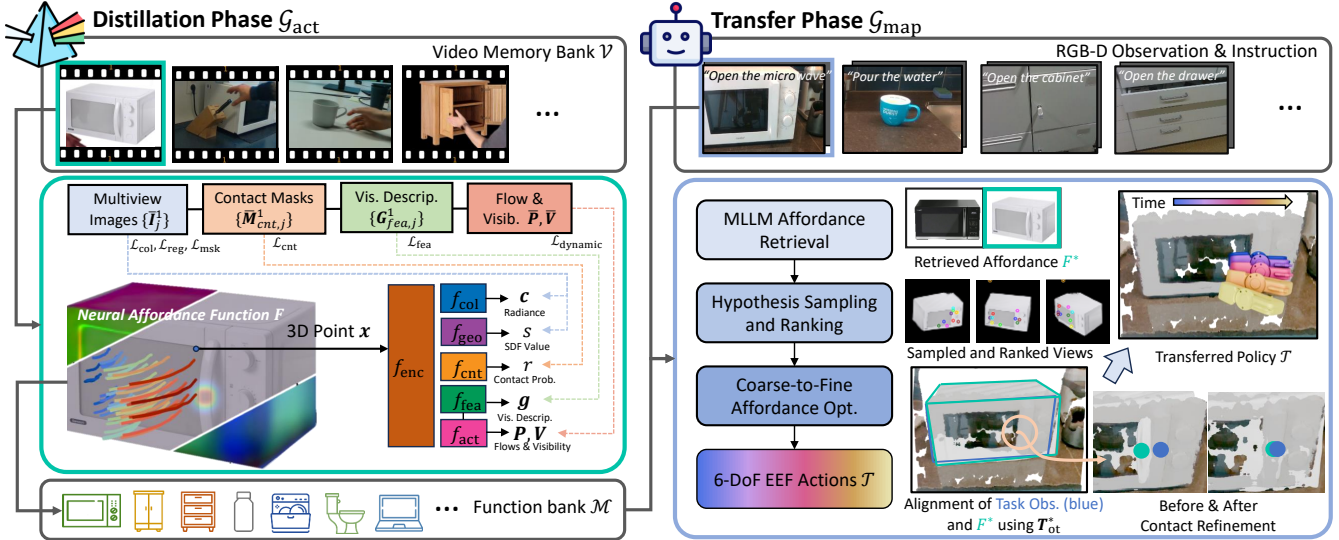


Fig. 2: Overview of **ACTRON3D** framework. In the distillation phase, multimodal knowledge from RGB videos is encoded into Neural Affordance Functions, and at deployment, an optimization-based transfer module enables action generalization to novel scenes.

a selected 6-DoF manipulation policy decoded from  $\mathcal{M}$  to the current scene:  $\mathcal{T} = \mathcal{G}_{\text{map}}(\{\mathbf{I}, \mathbf{D}\}, l, \mathcal{M})$  (Sect. III-D).

### B. Preliminaries

**Neural Signed Distance Function (NeuS).** We build on NeuS [41] and adopt an SDF-based geometric representation instead of 3D Gaussian Splats (3DGS) [42] for more accurate geometry reconstruction [43], forming the foundation for all other modalities. Formally, a *signed distance function* (SDF)  $\Omega : \mathbb{R}^3 \rightarrow \mathbb{R}$  maps a 3D point  $\mathbf{x}$  to its signed distance from the object surface:  $\mathcal{S} = \{\mathbf{x} \in \mathbb{R}^3 \mid \Omega(\mathbf{x}) = 0\}$ . This property enables realistic object modeling and improves affordance mapping. NeuS [41] uses standard volume rendering to render an attribute from any camera pose, computing the weight  $w(t)$  from the opaque density  $\rho(t)$  and accumulated transmittance  $T(t)$  between the near plane  $t_n$  and  $t$ .

$$w(t) = T(t) \rho(t), \quad T(t) = \exp \left( - \int_{t_n}^t \rho(u) \, du \right). \quad (1)$$

**Point Flows as Action Representation.** We use object-centric 3D point flows as the action representation, which is embodiment-agnostic, informative, and transferable [5, 6]. We denote point flows as  $\mathbf{P} \in \mathbb{R}^{N_q \times H \times 3}$ , where  $N_q$  stands for the number of points,  $H$  represents the horizon of flow, and the last dimension is the coordinate.

**6-DoF Manipulation Policy from Flows.** The flows implicitly encode dense actionable information of object movement, from which we extract a sequence of 6-DoF relative end-effector (EEF) poses, with respect to the initial pose. We first uniformly down-sample  $\mathbf{P}$  to a subset of flow  $\{\mathbf{p}_1, \dots, \mathbf{p}_{H'+1}\}$ , where each  $\mathbf{p}_t \in \mathbb{R}^{N_q \times 3}$  contains  $N_q$  key-points at timestep  $t$ . For each consecutive pair of  $(\mathbf{p}_t, \mathbf{p}_{t+1})$ , we aim to find the rigid transformation that fulfills:  $\mathbf{T}^* = \arg \min_{\mathbf{T} \in \text{SE}(3)} \sum_i^{N_q} w_i \|\mathbf{p}_{t+1}^i - \mathbf{T} \mathbf{p}_t^i\|^2$ , where  $w_i = \frac{1}{d_i + \beta}$  denotes the weight inversely proportional to the distance  $d_i$  between the key point  $i$  at the initial timestep and the gripper position, with  $\beta$  set to 0.1. We estimate the rigid

transformation leveraging the weighted SVD algorithm [44], yielding a sequence of relative  $\text{SE}(3)$  transformations  $\mathcal{T}_{\text{rel}} = \{\mathbf{T}_h^*\}_{h=1}^H$ . The absolute EEF trajectory  $\mathcal{T}$  is then obtained by composing the estimated  $\mathcal{T}_{\text{rel}}$  starting from the initial pose.

### C. Neural Functions Distillation from Videos

**Formulation.** We propose a 3D object-centric representation, *Neural Affordance Function* (NAF), that jointly encodes geometry, color, dense visual features, and affordance cues within a unified continuous function. Formally,  $F$  is parameterized by the following components with multiple MLPs:

$$\begin{aligned} F : \mathbb{R}^3 &\rightarrow \mathbb{R} \times \mathbb{R}^3 \times \mathbb{R}^d \times \mathbb{R} \times (\mathbb{R}^{H \times 3} \times \mathbb{R}^H), \\ F(\mathbf{x}) &= (f(\mathbf{f}_{\text{enc}}(\mathbf{x}), \mathbf{x}) \mid f \in \mathcal{F}), \quad \mathbf{x} \in \mathbb{R}^3, \\ \mathcal{F} &= \{\mathbf{f}_{\text{geo}}, \mathbf{f}_{\text{col}}, \mathbf{f}_{\text{fea}}, \mathbf{f}_{\text{cnt}}, \mathbf{f}_{\text{act}}\}. \end{aligned} \quad (2)$$

For a 3D point  $\mathbf{x}$ , the encoder head  $\mathbf{f}_{\text{enc}}$  produces a latent geometry feature  $\mathbf{z} \in \mathbb{R}^{256}$ , which serves as a shared backbone for other heads. Conditioned on  $\mathbf{z}$ , the geometry head  $\mathbf{f}_{\text{geo}}$  predicts the signed distance  $s \in \mathbb{R}$ , and the color head  $\mathbf{f}_{\text{col}}$  outputs RGB radiance  $\mathbf{c} \in \mathbb{R}^3$ . Although less critical for manipulation, color is retained for compatibility with vision foundation models. The feature head  $\mathbf{f}_{\text{fea}}$  generates  $d$ -dimensional visual descriptors  $\mathbf{g} \in \mathbb{R}^d$  [45] for robust affordance knowledge retrieval and alignment, while the contact head  $\mathbf{f}_{\text{cnt}}$  estimates the probability  $r \in \mathbb{R}$  that  $\mathbf{x}$  lies on a feasible contact region. Notably, both  $\mathbf{f}_{\text{fea}}$  and  $\mathbf{f}_{\text{cnt}}$  take  $\mathbf{x}$  in addition to  $\mathbf{z}$  as input. The action head  $\mathbf{f}_{\text{act}}$ , defined on the surface  $S$ , maps each surface point  $\mathbf{x}' \in \mathbb{S}^2$ , augmented with its queried geometric feature  $\mathbf{z}' = \mathbf{f}_{\text{enc}}(\mathbf{x}')$  and visual feature  $\mathbf{g}' = \mathbf{f}_{\text{fea}}(\mathbf{x}')$ , to  $H$ -step flows  $\mathbf{P} \in \mathbb{R}^{H \times 3}$  with visibility scores  $\mathbf{V} \in \mathbb{R}^H$ . Hence, we rewrite the  $\mathbf{f}_{\text{act}}$  defined in Eq. 2 as:  $(\mathbf{P}, \mathbf{V}) = \mathbf{f}_{\text{act}}(\mathbf{z}', \mathbf{g}', \mathbf{x}')$ . Restricting  $\mathbf{f}_{\text{act}}$  to the surface avoids volumetric redundancy and ensures a compact representation of motion knowledge. Conditioning action flows on both geometric and visual features increases

distinctiveness and mitigates collapse under imbalanced supervision, since valid flows occur on a small subset of the space. Unlike previous 2D affordance representations without spatial awareness [2–4], NAF operates directly in 3D, eliminating pixel-space ambiguity and enabling differentiable affordance optimization via continuous queries to  $F$ .

**Multimodal Differentiable Rendering.** NAF enables rendering any modality defined in volumetric space at arbitrary viewpoints using volume rendering:

$$Q_{m,u} = \int_{t_n}^{t_f} w(t) f_m(\mathbf{r}(t)) dt. \quad (3)$$

As depicted in Eq. 3,  $w(t)$  is the volumetric weight defined in Eq. 1 at depth  $t$  on ray  $\mathbf{r}$ , and  $Q_{m,u}$  is the 2D rendering of modality  $m$ . For a pixel  $u$ , we cast a ray  $\mathbf{r}(t)$  sampling encoded point-wise 3D function values  $f_m(\mathbf{r}(t))$  from near to far planes  $t_n$  and  $t_f$ , where  $m$  denotes the volume-distributed modality, i.e.,  $m \in \{\text{geo, col, fea, cnt}\}$ . The corresponding 2D rendering, e.g., visual descriptor  $Q_{\text{fea},u}$  or contact validity  $Q_{\text{cnt},u}$  is obtained via volume composition. Such a unified rendering scheme makes it possible to compare different modalities consistently across viewpoints, a key to bridging instance and viewpoint gaps.

**Multimodal Knowledge Extraction.** Given a video with an accompanying narration  $(\hat{V}, \hat{l})$ , we first capture the static state of the object. The initial hands-free frame  $\bar{I}^1$  is passed through an image-to-3D model [29] to generate six multi-view, pose-consistent images  $\{\bar{I}_j^1\}_{j=1}^6$  and their corresponding foreground masks  $\{\bar{M}_j^1\}_{j=1}^6$  [46], along with dense features  $\{\bar{G}_{\text{fea},j}^1\}_{j=1}^6$  extracted using a pretrained DINO [45].

To extract affordance cues, i.e., contact regions and point flows, the video  $\hat{V}$  is processed through a SfM pipeline [47] and a metric depth estimator [48], yielding per-frame camera extrinsics and dense depth maps. Following prior works [2, 3], we identify the first contact frame  $k_c > 1$  and its corresponding contact regions. Pixels from these regions are warped to the initial hands-free frame using the recovered camera parameters and dense depth, yielding contact masks aligned with the first view and its novel-view counterparts  $\{\bar{M}_{\text{cnt},j}^1\}_{j=1}^6$ . We track  $N_q$  keypoints sampled within the object’s foreground mask using a 3D point tracker [49]. This yields 3D point flows expressed in the coordinate frame of the first image, along with their visibility indicators:  ${}^c\mathbf{P} \in \mathbb{R}^{N_q \times H \times 3}$ ,  $\mathbf{V} \in \mathbb{R}^{N_q \times H}$ .

Since the flow  ${}^c\mathbf{P}$  is expressed in the camera frame, we estimate a similarity transformation  $T_{\text{oc}} \in \text{SIM}(3)$  to map it to the object’s canonical frame defined for NAF. Rotation and translation are initialized by perturbing the object’s principal axes and selecting the pose with the lowest average SDF value, while scale is initialized from the diagonal length of the bounding box of the object point cloud  ${}^c\mathcal{X}$ . The optimal pose is obtained by minimizing SDF values over the transformed object points:  $T_{\text{oc}}^* = \arg \min_{T_{\text{oc}}} \sum_{\mathbf{x} \in {}^c\mathcal{X}} \|f_{\text{geo}}(f_{\text{enc}}(T_{\text{oc}}\mathbf{x}), T_{\text{oc}}\mathbf{x})\|$ . Finally, the extracted flow is transformed to the object’s canonical space and used as supervision labels:  $\mathbf{P} = T_{\text{oc}}^* {}^c\mathbf{P}$ .

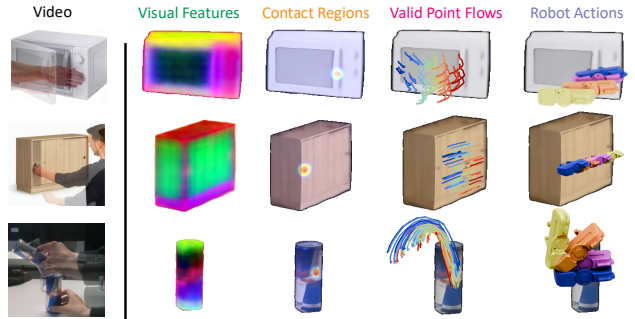


Fig. 3: Multimodal information and robot actions synthesized from novel views of NAFs fit to diverse videos.

**Neural Function Fitting.** The fitting process is split into two phases: first, we obtain geometric and visual understanding (*static phase*); then, we extract the object’s surface to constrain action flows within a bounded space (*dynamic phase*).

**Static Phase.** All heads except the action one are fitted as:

$$\mathcal{L}_{\text{static}} = \mathcal{L}_{\text{col}} + \lambda_1 \mathcal{L}_{\text{reg}} + \lambda_2 \mathcal{L}_{\text{msk}} + \lambda_3 \mathcal{L}_{\text{fea}} + \lambda_4 \mathcal{L}_{\text{cnt}}, \quad (4)$$

where color loss  $\mathcal{L}_{\text{col}}$ , regression loss  $\mathcal{L}_{\text{reg}}$ , and mask loss  $\mathcal{L}_{\text{msk}}$  follow NeuS [41]. We render  $Q_{\text{fea},u}$ ,  $Q_{\text{cnt},u}$  via Eq. 3 and compare them to the labels  $\bar{Q}_{\text{fea},u}$ ,  $\bar{Q}_{\text{cnt},u}$  for each pixel  $u$  sampled from the image plane  $\mathcal{U}$ . Specifically,  $\mathcal{L}_{\text{cnt}}$  is computed with the binary cross-entropy (BCE) loss.

$$\mathcal{L}_{\text{feat}} = \sum_{u \in \mathcal{U}} \|\bar{G}_{\text{fea},u} - Q_{\text{fea},u}\|^2, \quad (5)$$

$$\mathcal{L}_{\text{cnt}} = \sum_{u \in \mathcal{U}} \text{BCE}(\bar{M}_{\text{cnt},u}, Q_{\text{cnt},u}). \quad (6)$$

**Dynamic Phase.** With the other heads frozen, the action head is fitted using:

$$\mathcal{L}_{\text{dynamic}} = \sum_i \|\bar{P}_i - P_i\|^2 + \|\bar{V}_i - V_i\|^2, \quad (7)$$

where  $\bar{P}_i$ ,  $\bar{V}_i$  are the ground-truth flows and visibility, and  $P_i$ ,  $V_i$  are the corresponding predictions.

#### D. Affordance Transfer via Neural Functions

Each fitted neural affordance function  $F$  is paired with a language narration  $\hat{l}$  and stored in a function bank  $\mathcal{M}$ . At test time, given a new task specified by an RGB-D observation  $\{\mathbf{I}, \mathbf{D}\}$  and a natural-language instruction  $l$ , we extract a task feature map  $G_{\text{fea}}^t$  and transfer the action knowledge encoded in the best-matched affordance function  $F^*$  to the target scene. The transfer is realized by estimating a  $\text{SIM}(3)$  transformation  $T_{\text{ot}}^*$  that aligns  $F^*$  with the task observation geometrically and semantically by querying  $f_{\text{geo}}$ ,  $f_{\text{fea}}$  and  $f_{\text{cnt}}$ . Once aligned,  $f_{\text{cnt}}$  and  $f_{\text{act}}$  of  $F^*$  can be directly queried and converted into an executable action plan  $\mathcal{T}$ . We demonstrate several distilled NAFs in Fig. 3.

**Affordance Knowledge Retrieval.** We use a Multimodal Large Language Model (MLLM) [50] to retrieve the best-matched NAF  $F^*$ , by comparing the task observation and instruction with NAFs in the function bank. Unlike CLIP-based retrieval used in prior work [4], which computes visual and textual similarities in separate embedding spaces, the MLLM performs joint reasoning over paired multimodal

inputs. For each stored function  $F_i$ , we construct a descriptor  $\mathcal{O}_i = \{\bar{I}_i^1, \hat{l}_i\}$  consisting of each video's first hand-free frame and its associated narration. Given a task query  $\mathcal{C} = \{\mathbf{I}, l\}$ , we batch all descriptors  $\{\mathcal{O}_i\}_{i=1}^{N_V}$  as candidate options and prompt the MLLM to select the one most consistent with the query. This formulation allows exploiting both fine-grained visual appearance (e.g., shape) and high-level linguistic context (e.g., "open the *top* drawer" versus "open the *bottom* drawer"), enabling more precise retrieval across object instances and affordance types.

**Contact-Guided Hypothesis Sampling and Ranking.** We sample  $N_r$  view hypotheses from evenly spaced viewpoints along a horizontal circle around the origin of the selected NAF  $F^*$ . By querying  $f_{\text{cnt}}$ , invalid viewpoints where contact regions are occluded are filtered out. Remaining feasible candidates are ranked by visual feature similarity to the target. Following Eq. 3, we render the feature map  $\mathbf{Q}_{\text{fea}}^i$  encoded in  $f_{\text{fea}}$  for each remaining viewpoint  $i$ , pairing them with the target feature map  $\mathbf{G}_{\text{fea}}^t$ . Dense correspondences are established via best-buddy matching [51], producing sets of pixel pairs  $\{(\mathbf{u}_{i,j}, \mathbf{u}_{t,j})\}_{j=1}^{N_i}$  between each candidate view  $i$  and the target view  $t$ , where  $N_i$  denotes the number of correspondences. We quantify similarity using  $\mathcal{L}_{\text{corr}} = \frac{1}{N_i} \sum_{j=1}^{N_i} \|\mathbf{u}_{i,j} - \mathbf{u}_{t,j}\|_2^2$ . The top  $k$  poses with the lowest  $\mathcal{L}_{\text{corr}}$  are selected for the subsequent pose optimization stage.

**Affordance Optimization.** We further propose a coarse-to-fine affordance optimization strategy that first achieves global alignment before refining task-specific contact regions, ensuring alignment between observation and demonstration. Directly optimizing for contacts often leads to local minima; therefore, we initially perform coarse alignment on the top- $k$  candidates with  $\mathcal{L}_{\text{coarse}} = \mathcal{L}_{\text{fea}} + \beta_1 \mathcal{L}_{\text{surf}} + \beta_2 \mathcal{L}_{\text{depth}}$ :

$$\mathcal{L}_{\text{fea}} = \sum_{\mathbf{u} \in \mathcal{U}} (1 - \cos(\mathbf{G}_{\text{fea}, \mathbf{u}}^t, \mathbf{Q}_{\text{fea}, \mathbf{u}})), \quad (8)$$

$$\mathcal{L}_{\text{surf}} = \sum_{\mathbf{x} \in {}^t \mathcal{X}} \mathcal{L}_{\text{huber}}(f_{\text{geo}}(\mathbf{f}_{\text{enc}}(\mathbf{T}_{\text{ot}} \mathbf{x}), \mathbf{T}_{\text{ot}} \mathbf{x}), \mathbf{0}), \quad (9)$$

$$\mathcal{L}_{\text{depth}} = \sum_{\mathbf{u} \in \mathcal{U}} \mathcal{L}_{\text{huber}}(\mathbf{D}_{\mathbf{u}}^t, \mathbf{D}_{\mathbf{u}}). \quad (10)$$

The feature term  $\mathcal{L}_{\text{fea}}$  is defined as the cosine similarity loss between the feature map  $\mathbf{Q}_{\text{fea}, \mathbf{u}}$  rendered by  $f_{\text{fea}}$  and the target feature map  $\mathbf{G}_{\text{fea}, \mathbf{u}}^t$ . The surface term  $\mathcal{L}_{\text{surf}}$  queries  $f_{\text{geo}}$  for SDF values of the transformed point cloud  $\mathbf{T}_{\text{ot}} \mathbf{x}$  obtained from the RGB-D observation. The depth term  $\mathcal{L}_{\text{depth}}$  measures the discrepancy between the rendered depth map  $\mathbf{D}_{\mathbf{u}}$  and the observed depth  $\mathbf{D}_{\mathbf{u}}^t$ . The coarse pose  $\mathbf{T}'_{\text{ot}}$  is obtained by minimizing the following energy function:  $\mathbf{T}'_{\text{ot}} = \arg \min_{\mathbf{T}_{\text{ot}}} \mathcal{L}_{\text{coarse}}$ .

Then, in the fine stage, we add contact refinement while preserving the feature-metric and geometric alignment:  $\mathcal{L}_{\text{fine}} = \mathcal{L}_{\text{fea}} + \beta_3 \mathcal{L}_{\text{cnt}} + \beta_4 \mathcal{L}_{\text{surf}}$ , where  $\mathcal{L}_{\text{cnt}}$  is defined as:

$$\mathcal{L}_{\text{cnt}} = \sum_{\mathbf{q} \in \mathcal{Q}_c} \min_{\mathbf{q}' \in \mathcal{Q}_c} \|\mathbf{q}' - \mathbf{T}_{\text{ot}} \mathbf{q}\|. \quad (11)$$

$\mathcal{Q}_c$  denotes the contact point set extracted using  $f_{\text{cnt}}$ , and  $\mathcal{Q}_c^t \subset {}^t \mathcal{X}$  represents the matches based on the cosine

similarity of visual features. The final alignment initialized with  $\mathbf{T}'_{\text{ot}}$  is given by  $\mathbf{T}_{\text{ot}}^* = \arg \min_{\mathbf{T}_{\text{ot}}} \mathcal{L}_{\text{fine}}$ . Notably, our framework can further incorporate additional energy, such as the non-collision constraint.

With the final alignment  $\mathbf{T}_{\text{ot}}^*$  established, point flows are obtained by querying  $f_{\text{act}}$  on the transformed target point cloud:  $(\mathbf{P}, \mathbf{V}) = f_{\text{act}}(\mathbf{f}_{\text{enc}}(\mathbf{T}_{\text{ot}} {}^t \mathcal{X}), \mathbf{f}_{\text{fea}}(\mathbf{T}_{\text{ot}} {}^t \mathcal{X}), \mathbf{T}_{\text{ot}} {}^t \mathcal{X})$ . The flows  $\mathbf{P}$  with valid visibility ( $\mathbf{V} > 0$ ) are aggregated into a set of relative end-effector poses  $\mathcal{T}_{\text{rel}}$ , as described in Sec. III-B. For robot execution, we determine the contact point as  $\mathbf{x}^* = \arg \max_{\mathbf{x} \in {}^t \mathcal{X}} f_{\text{cnt}}(\mathbf{f}_{\text{enc}}(\mathbf{T}_{\text{ot}} {}^t \mathbf{x}), \mathbf{T}_{\text{ot}} {}^t \mathbf{x})$  and employ a grasp detector [52] to estimate a 6-DoF grasp pose  $\hat{\mathbf{T}}$  by sampling candidate points around  $\mathbf{x}^*$ . The relative motions  $\mathcal{T}_{\text{rel}}$  are then composed with  $\hat{\mathbf{T}}$  to yield a sequence of absolute end-effector poses  $\mathcal{T} = \{\mathbf{T}_i\}_{i=1}^H$  for execution.

### E. Implementation Details

**Network Architecture.** The heads  $f_{\text{enc}}$ ,  $f_{\text{geo}}$ , and  $f_{\text{col}}$  share identical architectures as [41]. The feature head  $f_{\text{fea}}$  has an additional 12-level hash-grid encoding [53] and a 6-band positional encoding, followed by a 2-layer MLP for decoding. The contact head  $f_{\text{cnt}}$  uses the same positional encoding as  $f_{\text{fea}}$ , followed by a 3-layer MLP for decoding. Finally, the action head  $f_{\text{act}}$  takes surface points with a 10-band positional encoding, fuses them with  $\mathbf{g}$  and  $\mathbf{z}$  (compressed to a dimension of 96 by a 2-layer MLP), and processes the concatenated representation with a 3-layer MLP. All MLP modules have a hidden dimension of 128.

**Fitting Protocol.** In the *static phase*, we jointly optimize geometry, color, feature, and contact heads using Adam [54] with a learning rate of  $5 \times 10^{-4}$ . The loss weights are:  $\lambda_1 = \lambda_3 = 0.1$ ,  $\lambda_2 = 1.0$ ,  $\lambda_4 = 0.5$ . This stage runs for 3k iterations. In the *dynamic phase*, the action head is fitted while freezing the static components for an extra 600 iterations and a learning rate of  $1 \times 10^{-3}$ . For each manipulation task, we require only 2–3 demonstration videos—sourced from HOI datasets [9], generative models [10], or self-captured recordings—providing a significant advantage over retrieval-based methods like RAM [4], which typically demand an order of magnitude more demonstrations.

**Inference Protocol.** At inference, we select the top  $k = 3$  poses and use an Adam optimizer with a learning rate of  $1 \times 10^{-2}$  and weights  $\beta_2 = \beta_3 = 100$ ,  $\beta_1 = \beta_4 = 1000$  for affordance optimization. The coarse stage is run for 100 iterations, followed by 50 iterations of refinement.

## IV. EXPERIMENTS

Here, we demonstrate the following aspects of our method: 1) It outperforms several strong baseline models across various household tasks in both simulator and real-world settings. 2) Representing actionable knowledge as a continuous function provides more feasible and intuitive robot motion, leading to better performance. 3) Compared with 2D methods, lifting information into a 3D neural function achieves a performance gain by a large margin. 4) It can be deployed for several downstream applications seamlessly.

	<b>T01</b>	<b>T02</b>	<b>T03</b>	<b>T04</b>	<b>T05</b>	<b>T06</b>	<b>T07</b>	<b>T08</b>	<b>T09</b>	<b>T10</b>	<b>T11</b>	<b>T12</b>	<b>T13</b>	<b>Avg.</b>
Where2Act [17]	60.0	40.0	33.3	53.3	<b>100.0</b>	<b>100.0</b>	40.0	6.7	33.3	<b>40.0</b>	26.7	<b>100.0</b>	<b>100.0</b>	56.4
VRB <sup>†</sup> [2]	<b>60.0</b>	<b>60.0</b>	40.0	40.0	13.3	<b>100.0</b>	0.0	0.0	53.3	10.0	<b>53.3</b>	<b>93.3</b>	<b>100.0</b>	42.6
RAM [4]	46.7	<b>60.0</b>	33.3	53.3	13.3	93.3	33.3	<b>93.3</b> <sup>*</sup>	66.7 <sup>*</sup>	33.3 <sup>*</sup>	<b>53.3</b> <sup>*</sup>	80.0	80.0	58.5
GFlow [15]	6.7	13.3	20.0	33.3	20.0	<b>100.0</b>	<b>93.3</b>	0.0	13.3	0.0	20.0	<b>100.0</b>	<b>93.3</b>	39.6
VidBot [7]	46.7	<b>100.0</b>	<b>73.3</b>	<b>100.0</b>	26.7	<b>100.0</b>	33.3	<b>86.7</b>	<b>73.3</b>	<b>93.3</b>	46.7	<b>100.0</b>	<b>100.0</b>	75.9
<b>Ours</b>	<b>73.3</b>	<b>100.0</b>	<b>80.0</b>	<b>100.0</b>	<b>80.0</b>	<b>93.3</b>	<b>100.0</b>	<b>93.3</b>	<b>86.7</b>	<b>93.3</b>	<b>73.3</b>	<b>100.0</b>	<b>100.0</b>	<b>90.8</b>

TABLE I: Quantitative results on tasks evaluated in simulators on success rate (%). **T01**: Open drawer **T02**: Close drawer, **T03**: Open microwave, **T04**: Close microwave, **T05**: Open hinge cabinet, **T06**: Close hinge cabinet, **T07**: Open dishwasher, **T08**: Open slide cabinet, **T09**: Close slide cabinet, **T10**: Close laptop lid, **T11**: Put down toilet seat: **T12**: Pick up cup, **T13**: Pick up bottle. <sup>\*</sup> uses self-collected data for novel tasks. <sup>†</sup> uses strategy from [4] to lift affordance to 3D.

	<b>RT01</b>	<b>RT02</b>	<b>RT03</b>	<b>RT04</b>	<b>RT05</b>	<b>Avg.</b>
RAM	40.0	20.0	60.0	0.0 <sup>*</sup>	40.0 <sup>*</sup>	32.0
VidBot	60.0	<b>40.0</b>	<b>100.0</b>	0.0	50.0	50.0
<b>Ours</b>	<b>70.0</b>	<b>70.0</b>	<b>90.0</b>	<b>80.0</b>	<b>70.0</b>	<b>76.0</b>

TABLE II: Real-world experiment results on selected tasks. **RT01**: Open drawer, **RT02**: Open microwave, **RT03**: Close microwave, **RT04**: Pour water, **RT05**: Wiping table with sponge. <sup>\*</sup>: Use self-collected data for retrieval.

### A. Experiment Setup

**Simulator Setup.** We use RLBench [55] as the simulation environment, deploying a *Franka-Emika Panda* to interact with target objects. Our evaluation covers 13 RLBench tasks that involve manipulating both articulated and portable objects. For each task, we assess performance under three different viewpoints, generating five trajectories per viewpoint, resulting in a total of 15 trials per method. Following prior works [4, 7, 15], we report the success rate (SR) (%) as the primary evaluation metric. A trial is considered successful if the robot’s end-effector manipulates the target object along the intended DoF beyond a predefined threshold.

**Real Robot Setup.** We conduct real-world manipulation experiments in previously unseen human-suited environments. The test platform is a physical *Hello Robot Stretch 3* equipped with an on-board RGB-D camera for perception.

**Baseline Models.** We compare against five representative baselines for 2D/3D affordance prediction. **Where2Act** [17] learns 3D actionable affordance from simulated articulated objects, while **VRB** [2] trains on large-scale human videos to predict 2D affordance on the image plane. **RAM** [4], like our method, follows a retrieve-and-transfer scheme: however, it only retrieves 2D affordances, matches them pixel-wise, and lifts them to 3D using clustered surface normals as geometric priors. **GFlow** [15] and **VidBot** [7] both learn 3D affordance from egocentric videos; **GFlow** outputs full 6-DoF poses but requires manual input of contact regions, while **VidBot** removes this dependency but produces only 3D waypoints. In contrast, our method predicts dense 6-DoF end-effector poses without requiring any human intervention.

### B. Results and Discussions

**Simulator Benchmark.** As shown in Tab. I, our method achieves the highest overall success rate of 90.8%, representing a 14.9 pp improvement over the runner-up [7]. Among the baselines, **Where2Act** performs well on tasks involving hinge-articulated and portable objects but exhibits limited generalization to novel objects. 2D affordance prediction methods, **VRB** and **RAM**, achieve performance comparable

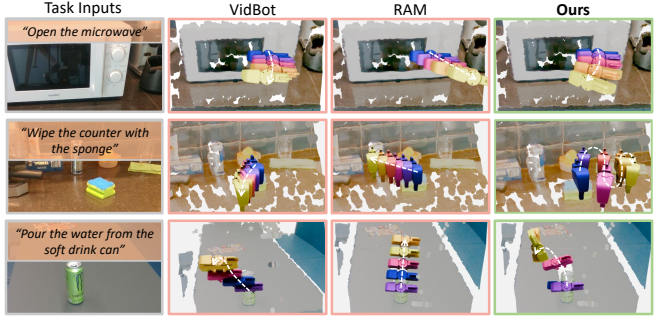


Fig. 4: Inferred robot gripper actions by different methods.

to **Where2Act** on simpler tasks; however, they struggle significantly on articulated objects requiring complex, curved 3D motions, such as door-opening in **T03** and **T05**. This failure stems from oversimplified 2D motion cues, which lead to infeasible linear motions and frequent gripper slips during execution. 3D affordance prediction methods, such as **GFlow** and **VidBot**, achieve notable improvements over 2D-based methods, particularly on tasks demanding complex motion. Nevertheless, their performance varies substantially across tasks (e.g., **T05** vs. **T11**), primarily due to the scale and diversity of their training datasets. These results emphasize the importance of 3D affordance representations for everyday object manipulation. Existing methods remain limited by their reliance on large datasets for generalization. In contrast, our approach captures functional similarities across objects through a compact neural representation while accounting for geometric and visual differences via an intuitive optimization scheme. As a result, it produces more feasible, scale-aware motion trajectories, reducing gripper slip and achieving higher success rates.

**Real Robot Experiments.** We evaluated our method on five real-world tasks, performing 10 trials for each and comparing against **RAM** (retrieval-based) and **VidBot** (prediction-based). As shown in Tab. II, our approach achieves an average SR of 76%. Notably, only our method generated full 6-DoF motions, essential for tasks like pouring, whereas baselines were limited to purely translational motions, resulting in potential grasp slip and task failures (Fig. 4).

### C. Ablation Studies

We conducted detailed ablation experiments on a subset of tasks to study the impact of each key component of our pipeline. The results are summarized in Tab. III. **V1** replaces NAF with direct 2D feature-based match and transfer [4]. **V2** removes contact-guided initialization, and **V3** disables feature-based ranking. **V4** bypasses optimization and trans-

	<b>AT01</b>	<b>AT02</b>	<b>AT03</b>	<b>AT04</b>	<b>AT05</b>	<b>AT06</b>	<b>Avg.</b>
<b>Ours [Full Model]</b>	<b>73.3</b>	<b>100.0</b>	<b>80.0</b>	<b>100.0</b>	<b>93.3</b>	<b>73.3</b>	<b>86.7</b>
w/o Neural Function [V1]	66.7	26.7	73.3	0.0	6.7	6.7	30.0
w/o Contact Sampling [V2]	53.3	13.3	26.7	73.3	<b>100.0</b>	<b>73.3</b>	56.6
w/o Viewpoint Ranking [V3]	66.7	33.3	0.0	<b>100.0</b>	<b>100.0</b>	46.7	57.8
w/o Afford. Optimization [V4]	<b>73.3</b>	0.0	0.0	26.7	20.0	6.7	21.1
w/o Contact Refinement [V5]	66.7	<b>66.7</b>	33.3	66.7	<b>100.0</b>	<b>66.7</b>	66.7

TABLE III: Ablation results on 6 selected tasks. **AT01**: Open drawer, **AT02**: Close drawer, **AT03**: Open microwave, **AT04**: Close microwave, **AT05**: Open slide cabinet. **AT06**: Put down toilet seat. <sup>†</sup>: Use strategy from [4] to lift affordance to 3D.

fers affordance from the most similar retrieved view, while **V5** removes the contact-centric refinement stage.

**Impact of Neural Representation (V1):** We demonstrate the effectiveness of embedding action-related information within a neural function. In **V1**, performance drops by over 50%, which is expected as large viewpoint gaps between demonstration and task scenes make direct transfer unreliable. Without a functional representation, the system cannot leverage multimodal optimization for robust affordance alignment, leading to significant degradation.

**Impact of Initialization Strategy (V2-V3):** In **V2**, disabling contact-guided sampling allows infeasible poses to enter the optimization module, increasing susceptibility to local minima and reducing SR by 30%. In **V3**, removing the ranking module reduces SR by 28.9%, as relying solely on geometric plausibility often results in suboptimal initialization. This underscores the critical role of feature-informed ranking in guiding the optimizer toward feasible and high-quality poses.

**Impact of Optimization Scheme (V4-V5):** Disabling the entire optimization (**V4**) and transferring affordance solely from the most similar views reduces SR drastically to 21.1%. This sharp drop indicates that sparse 2D visual alignment, without 3D geometric alignment, is insufficient for handling large viewpoint variations due to the gaps between the selected view and the target scene. Removing the final contact-centric refinement (**V5**) results in a SR decline to 66.7%, as global alignment from the first stage cannot ensure precise alignment in the contact area, where the desired actionable flows reside. This highlights the necessity of contact-constrained refinement for accurate motion execution.

#### D. Downstream Applications

We further showcase the versatility of ACTRON3D by applying it to a range of downstream applications.

**Long-horizon Manipulation.** ACTRON3D can be seamlessly integrated into MLLM-based task and motion planning frameworks [56], enabling flexible and complex manipulation from free-form language instructions. Given an instruction, the MLLM [50] produces a high-level plan as a sequence of sub-tasks. For each step, ACTRON3D retrieves the corresponding NAF, aligns it with the current observation, and executes the action. As demonstrated in Fig. 1, the given instruction “*Use the sponge in the drawer to clean the table*” is decomposed into three sub-tasks and executed sequentially, demonstrating our framework’s ability to support more complex manipulation tasks.

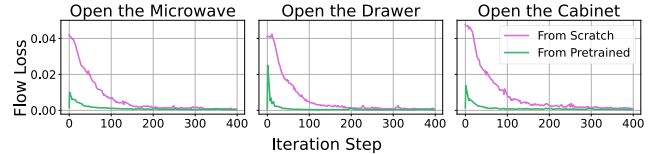


Fig. 5: Loss curves of the action head when trained from scratch vs. initialized with pretrained weights of the retrieved NAF model.

**Policy Fine-tuning.** During deployment, the action head  $f_{\text{act}}$  of the retrieved NAF can be further optimized online for *previously unseen objects*, using observations collected from successful executions. We evaluated this procedure on tasks **T01**, **T03**, and **T05** under the same settings as discussed in Sec. IV, achieving absolute SR improvements of 6.7%, 13.3%, and 6.7%, respectively. These gains arise because fine-tuning with local motion data helps correct errors from SfM and monocular depth estimation, thereby improving overall performance. Moreover, convergence is accelerated by around  $\times 4$  (Fig. 5): fine-tuning reaches convergence within  $\sim 100$  steps, whereas training from scratch requires around 400 steps. Taken together, these results further validate that the latent features encoded by NAF provide representations directly beneficial for action learning.

## V. CONCLUSION

We introduce ACTRON3D, a framework for zero-shot robotic manipulation that learns object-centric affordance representations from monocular videos and transfers them to novel objects, viewpoints, and embodiments. Central to our approach is the *Neural Affordance Function*, a neural representation that jointly encodes geometry, features, contact priors, and point flows to decode manipulation skills. With an optimization-based transfer pipeline—combining MLLM-based affordance retrieval and coarse-to-fine optimization—ACTRON3D enables embodiment-agnostic generalization without reliance on large-scale teleoperated demonstrations. Our pipeline resolves the inherent ambiguity of 2D cues in prior works, improves data efficiency, and bridges viewpoint discrepancies. With a few video demonstrations, our framework consistently surpasses strong baselines on diverse household tasks, both in simulation and the real world, underscoring its strong scalability and generalizability.

**Limitations and Future Works.** Our method uses recent 3D AIGC techniques [29] to infer knowledge from unseen views; however, artifacts in these generated views can negatively impact the action head. Moreover, inference relies on iterative optimization and thus cannot meet strict low-latency requirements. Future work will investigate acceleration strategies to enhance deployment efficiency, including vectorized optimization [57] and second-order solvers [58].

## REFERENCES

- [1] S. S. Jones, “Imitation in infancy: The development of mimicry,” *Psychological science*, vol. 18, no. 7, pp. 593–599, 2007.
- [2] S. Bahl, R. Mendonca, L. Chen, U. Jain, and D. Pathak, “Affordances from human videos as a versatile representation for robotics,” in *CVPR*, 2023.
- [3] Y. Ju, K. Hu, G. Zhang, G. Zhang, M. Jiang, and H. Xu, “Robo-abc: Affordance generalization beyond categories via semantic correspondence for robot manipulation,” 2024, arXiv:2401.07487.

[4] Y. Kuang, J. Ye, H. Geng, J. Mao, C. Deng, L. Guibas, H. Wang, and Y. Wang, “Ram: Retrieval-based affordance transfer for generalizable zero-shot robotic manipulation,” 2024, arXiv:2407.04689.

[5] M. Xu, Z. Xu, Y. Xu, C. Chi, G. Wetzstein, M. Veloso, and S. Song, “Flow as the cross-domain manipulation interface,” in *CoRL*, 2024.

[6] H. Bharadhwaj, R. Mottaghi, A. Gupta, and S. Tulsiani, “Track2act: Predicting point tracks from internet videos enables diverse zero-shot robot manipulation,” *arXiv preprint arXiv:2405.01527*, 2024.

[7] H. Chen, B. Sun, A. Zhang, M. Pollefeys, and S. Leutenegger, “Vidbot: Learning generalizable 3d actions from in-the-wild 2d human videos for zero-shot robotic manipulation,” *CVPR*, 2025.

[8] G. Papagiannis, N. D. Palo, P. Vitiello, and E. Johns, “R+x: Retrieval and execution from everyday human videos,” *ICRA*, 2025.

[9] Y. Liu, Y. Liu, C. Jiang, K. Lyu, W. Wan, H. Shen, B. Liang, Z. Fu, H. Wang, and L. Yi, “Hoi4d: A 4d egocentric dataset for category-level human-object interaction,” in *CVPR*, June 2022, pp. 21 013–21 022.

[10] KuaiShou’s Large Model Algorithm Team, “KlingAI,” 2024, accessed: 22 August 2025. [Online]. Available: <https://app.klingai.com>

[11] L. Yen-Chen, P. Florence, J. T. Barron, A. Rodriguez, P. Isola, and T.-Y. Lin, “iNeRF: Inverting neural radiance fields for pose estimation,” in *IROS*, 2021.

[12] C.-H. Lin, W.-C. Ma, A. Torralba, and S. Lucey, “Barf: Bundle-adjusting neural radiance fields,” in *ICCV*, 2021, pp. 5741–5751.

[13] H. Chen, F. Manhardt, N. Navab, and B. Busam, “Texpose: Neural texture learning for self-supervised 6d object pose estimation,” in *CVPR*, 2023, pp. 4841–4852.

[14] H. Chen, B. Xu, and S. Leutenegger, “Funcgrasp: Learning object-centric neural grasp functions from single annotated example object,” in *ICRA*. IEEE, 2024, pp. 1900–1906.

[15] C. Yuan, C. Wen, T. Zhang, and Y. Gao, “General flow as foundation affordance for scalable robot learning,” *CoRL*, 2024.

[16] S. Bahl, A. Gupta, and D. Pathak, “Human-to-robot imitation in the wild,” *arXiv preprint arXiv:2207.09450*, 2022.

[17] K. Mo, L. J. Guibas, M. Mukadam, A. Gupta, and S. Tulsiani, “Where2act: From pixels to actions for articulated 3d objects,” in *ICCV*, 2021, pp. 6813–6823.

[18] A. Myers, C. L. Teo, C. Fermüller, and Y. Aloimonos, “Affordance detection of tool parts from geometric features,” in *ICRA*, 2015, pp. 1374–1381.

[19] C.-Y. Chuang, J. Li, A. Torralba, and S. Fidler, “Learning to act properly: Predicting and explaining affordances from images,” in *CVPR*, 2018, pp. 975–983.

[20] T.-T. Do, A. Nguyen, and I. Reid, “Affordancenet: An end-to-end deep learning approach for object affordance detection,” in *ICRA*. IEEE, 2018, pp. 5882–5889.

[21] R. Wu, Y. Zhao, K. Mo, Z. Guo, Y. Wang, T. Wu, Q. Fan, X. Chen, L. Guibas, and H. Dong, “Vat-mart: Learning visual action trajectory proposals for manipulating 3d articulated objects,” 2022, arXiv:2106.14440.

[22] Y. Wang, R. Wu, K. Mo, J. Ke, Q. Fan, L. Guibas, and H. Dong, “AdaAfford: Learning to adapt manipulation affordance for 3d articulated objects via few-shot interactions,” *ECCV*, 2022.

[23] P. R. Florence, L. Manuelli, and R. Tedrake, “Dense object nets: Learning dense visual object descriptors by and for robotic manipulation,” *CoRL*, 2018.

[24] A. Rashid, S. Sharma, C. M. Kim, J. Kerr, L. Y. Chen, A. Kanazawa, and K. Goldberg, “Language embedded radiance fields for zero-shot task-oriented grasping,” in *CoRL*, 2023.

[25] W. Shen, G. Yang, A. Yu, J. Wong, L. P. Kaelbling, and P. Isola, “Distilled feature fields enable few-shot language-guided manipulation,” in *CoRL*, 2023.

[26] Q. Wang, H. Zhang, C. Deng, Y. You, H. Dong, Y. Zhu, and L. Guibas, “Sparsedff: Sparse-view feature distillation for one-shot dexterous manipulation,” 2024, arXiv:2310.16838.

[27] Y. Ze, G. Yan, Y.-H. Wu, A. Macaluso, Y. Ge, J. Ye, N. Hansen, L. E. Li, and X. Wang, “Gnfactor: Multi-task real robot learning with generalizable neural feature fields,” 2024, arXiv:2308.16891.

[28] Y. Wang, M. Zhang, Z. Li, T. Kelestemur, K. Driggs-Campbell, J. Wu, L. Fei-Fei, and Y. Li, “D<sup>3</sup>fields: Dynamic 3d descriptor fields for zero-shot generalizable rearrangement,” 2024, arXiv:2309.16118.

[29] X. Long, Y.-C. Guo, C. Lin, Y. Liu, Z. Dou, L. Liu, Y. Ma, S.-H. Zhang, M. Habermann, C. Theobalt, *et al.*, “Wonder3d: Single image to 3d using cross-domain diffusion,” 2023, arXiv:2310.15008.

[30] J. Xu, W. Cheng, Y. Gao, X. Wang, S. Gao, and Y. Shan, “Instantmesh: Efficient 3d mesh generation from a single image with sparse-view large reconstruction models,” 2024, arXiv:2404.07191.

[31] S. Nair, A. Rajeswaran, V. Kumar, C. Finn, and A. Gupta, “R3m: A universal visual representation for robot manipulation,” 2022, arXiv:2203.12601.

[32] T. Xiao, I. Radovanic, T. Darrell, and J. Malik, “Masked visual pre-training for motor control,” *arXiv preprint arXiv:2203.06173*, 2022.

[33] L. Smith, N. Dhawan, M. Zhang, P. Abbeel, and S. Levine, “Avid: Learning multi-stage tasks via pixel-level translation of human videos,” *arXiv preprint arXiv:1912.04443*, 2019.

[34] Y. Qin, Y.-H. Wu, S. Liu, H. Jiang, R. Yang, Y. Fu, and X. Wang, “Dexmv: Imitation learning for dexterous manipulation from human videos,” in *ECCV*. Springer, 2022, pp. 570–587.

[35] C. Wang, H. Shi, W. Wang, R. Zhang, L. Fei-Fei, and C. K. Liu, “Dexcap: Scalable and portable mocap data collection system for dexterous manipulation,” *arXiv preprint arXiv:2403.07788*, 2024.

[36] K. Shaw, S. Bahl, and D. Pathak, “Videodex: Learning dexterity from internet videos,” in *CoRL*. PMLR, 2023, pp. 654–665.

[37] S. Bahl, R. Mendonca, L. Chen, U. Jain, and D. Pathak, “Affordances from human videos as a versatile representation for robotics,” in *CVPR*, 2023, pp. 13 778–13 790.

[38] J. Liang, R. Liu, E. Ozguroglu, S. Sudhakar, A. Dave, P. Tokmakov, S. Song, and C. Vondrick, “Dreamitate: Real-world visuomotor policy learning via video generation,” 2024, arXiv:2406.16862.

[39] H. Bharadhwaj, D. Dwibedi, A. Gupta, S. Tulsiani, C. Doersch, T. Xiao, D. Shah, F. Xia, D. Sadigh, and S. Kirmani, “Gen2act: Human video generation in novel scenarios enables generalizable robot manipulation,” 2024, arXiv:2409.16283.

[40] S. Patel, S. Mohan, H. Mai, U. Jain, S. Lazebnik, and Y. Li, “Robotic manipulation by imitating generated videos without physical demonstrations,” *arXiv preprint arXiv:2507.00990*, 2025.

[41] P. Wang, L. Liu, Y. Liu, C. Theobalt, T. Komura, and W. Wang, “Neus: Learning neural implicit surfaces by volume rendering for multi-view reconstruction,” *NeurIPS*, 2021.

[42] B. Kerbl, G. Kopanas, T. Leimkühler, and G. Drettakis, “3d gaussian splatting for real-time radiance field rendering,” *ACM Transactions on Graphics*, vol. 42, no. 4, July 2023.

[43] H. Xia, E. Su, M. Memmel, A. Jain, R. Yu, N. Mbiziwo-Tiapo, A. Farhadi, A. Gupta, S. Wang, and W.-C. Ma, “Drawer: Digital reconstruction and articulation with environment realism,” in *CVPR*, 2025.

[44] P. Besl and N. D. McKay, “A method for registration of 3-d shapes,” *TAPMI*, vol. 14, no. 2, pp. 239–256, 1992.

[45] M. Oquab, T. Darct, T. Moutakanni, H. Vo, M. Szafrańiec, V. Khalidov, P. Fernandez, D. Haziza, F. Massa, A. El-Nouby, *et al.*, “Dinov2: Learning robust visual features without supervision,” 2023, arXiv:2304.07193.

[46] A. Kirillov, E. Mintun, N. Ravi, H. Mao, C. Rolland, L. Gustafson, T. Xiao, S. Whitehead, A. C. Berg, W.-Y. Lo, *et al.*, “Segment anything,” in *ICCV*, 2023, pp. 4015–4026.

[47] Z. Li, R. Tucker, F. Cole, Q. Wang, L. Jin, V. Ye, A. Kanazawa, A. Holynski, and N. Snavely, “Megasam: Accurate, fast, and robust structure and motion from casual dynamic videos,” in *CVPR*, 2024.

[48] L. Piccinelli, C. Sakaridis, Y.-H. Yang, M. Segu, S. Li, W. Abbeloos, and L. V. Gool, “UniDepthV2: Universal monocular metric depth estimation made simpler,” 2025, arXiv:2502.20110.

[49] B. Zhang, L. Ke, A. W. Harley, and K. Fragkiadaki, “Tapip3d: Tracking any point in persistent 3d geometry,” 2025, arXiv:2504.14717.

[50] OpenAI, “Gpt-4o system card,” 2024, arXiv:2410.21276.

[51] S. Amir, Y. Gandelsman, S. Bagon, and T. Dekel, “Deep vit features as dense visual descriptors,” *ECCVW What is Motion For?*, 2022.

[52] H.-S. Fang, C. Wang, H. Fang, M. Gou, J. Liu, H. Yan, W. Liu, Y. Xie, and C. Lu, “Anygrasp: Robust and efficient grasp perception in spatial and temporal domains,” *T-RO*, 2023.

[53] T. Müller, A. Evans, C. Schied, and A. Keller, “Instant Neural Graphics Primitives with Multiresolution Hash Encoding,” *ACM ToG*, 2022.

[54] D. P. Kingma and J. Ba, “Adam: A method for stochastic optimization,” *arXiv preprint arXiv:1412.6980*, 2014.

[55] S. James, Z. Ma, D. Rovick Arrojo, and A. J. Davison, “Rlbench: The robot learning benchmark & learning environment,” *RA-L*, 2020.

[56] Z. Yang, C. Garrett, D. Fox, T. Lozano-Pérez, and L. P. Kaelbling, “Guiding long-horizon task and motion planning with vision language models,” in *ICRA*, 2025, pp. 16 847–16 853.

[57] X. Kong, S. Liu, M. Taher, and A. J. Davison, “vmap: Vectorised object mapping for neural field slam,” 2023, arXiv:2302.01838.

[58] L. Höllerin, A. Božič, M. Zollhöfer, and M. Nießner, “3dgs-lm: Faster gaussian-splatting optimization with levenberg-marquardt,” 2025, arXiv:2409.12892.